

A comprehensive model for predicting droplet freezing features on a cold substrate

Moussa Tembely^{1,†} and Ali Dolatabadi^{1,†}

¹Department of Mechanical, Industrial, and Aerospace Engineering, Concordia University,
1515 Ste-Catherine Street West, H3G 1M8, Montreal, Quebec, Canada

(Received 3 July 2018; revised 9 October 2018; accepted 12 October 2018;
first published online 21 November 2018)

Water droplet freezing affects many aspects of our daily lives, although there is no comprehensive model which retrieves all of the experimentally observed features when a liquid water droplet deposited on a cold substrate turns to ice. In this paper, we present general governing equations to describe water droplet freezing on a solid substrate by accounting for the physical properties of each phase present, namely the liquid and ice, in addition to the solid substrate. The approach, which takes advantage of the full mean curvature expression of both the droplet–air and liquid–ice interfaces, disjoining pressure, the Gibbs–Thomson effect, natural convection and the substrate thermal and physico-chemical properties, enables us to model a more realistic frozen droplet shape, without a prior assumption for the freezing growth angle. In addition to correctly predicting the freezing time, we capture both qualitatively and quantitatively the key experimentally observed features during water droplet freezing such as volume expansion, concave ice front and the cusp singularity. Furthermore, the proposed equation for the tip angle seems to explain its experimentally observed variability.

Key words: drops, multiphase flow, icing

1. Introduction

Water droplet freezing is well known to significantly affect many practical situations of our daily lives, especially in cold weather regions. In the aerospace industry, icing is a central economic and safety issue, as ice formation on an aircraft wing increases the drag while the ability of the airfoil to create lift is decreased. Conditions to prevent ice formation and a better understanding of the physics governing the icing phenomenon are highly intertwined, and are the focus of much current research (Jung *et al.* 2012; Potapczuk 2013; Hao, Lv & Zhang 2014; Mohammadi, Tembely & Dolatabadi 2017; Tembely, Attarzadeh & Dolatabadi 2018). In spite of the wide range of applications, the numerical or theoretical modelling and validation of a single water droplet freezing with all the features experimentally observed (Enríquez *et al.* 2012), ranging from the curved freezing front to the cusp formation, are yet to be fully addressed.

[†] Email addresses for correspondence: moussa.tembely@concordia.ca,
ali.dolatabadi@concordia.ca

The challenge and the modelling complexity, under the continuum hypothesis, are to capture the sharp moving solid–liquid interface across which the material properties change. The first icing code model was developed by Messinger (1953); more recently an extended Messinger model has been developed by Özgen & Canıbek (2008). The early work on droplet spreading and solidification was carried out by Madejski (1976). His analytical development provides an estimation of the spreading diameter (or the degree of flattening) during solidification by combining the Stefan problem (Carslaw & Jaeger 1959) and a simple radial flow assumption. His model, based on an axisymmetric flow assumption of the velocity field, was improved in Delplanque & Rangel (1997) using a more suitable approximation for both the velocity field and the dissipation. These models applied to metals usually do not account for density difference between the liquid and solid state. Actually, there are very few publications addressing theoretically and/or numerically water droplet freezing apart from the pioneering works by Anderson, Worster & Davis (1996) based on a geometrical analysis which describes the cusp formation with a generalization relaxing the flat solid–liquid interface condition in Schultz, Worster & Anderson (2001), and the subsequent use of the thin film approach (Myers, Charpin & Chapman 2002; Myers & Charpin 2004; Zdražil, Stepanek & Matar 2006), and the boundary integral technique (Ajaev & Davis 2003, 2004). Ajaev & Davis (2004) even showed, by accounting for the Gibbs–Thomson effect, that a consistent solution of the governing equation can be recovered using an arbitrary value for the contact angles at the tri-junction point. However, in their model, the interactions of the droplet with a substrate or the surrounding gas are neglected. In addition no comparison is provided with respect to experiments. It is worth noting that extensive work has been performed on defining the interface, based on the Stefan problem or crystallization kinematics (Zhang *et al.* 2004), however the geometric approach inferring the shape of the droplet is not considered.

The approach in Anderson *et al.* (1996) has been recently used by Snoeijer & Brunet (2012) for analysing the singularity at the tip of a freezing water droplet, yet the more challenging curved freezing front, the liquid (water) and solid (ice) interface, is not considered nor is the interaction with the substrate as well as the surrounding gas. However, recently, an interesting model by Marín *et al.* (2014) has been proposed to address the tip formation by assuming the droplet to be thermally isolated, and the local analysis of the tip formation suggests a universal behaviour in terms of the tip cone angle and the angle between the freezing front and the liquid–air interface. However, these models account neither for the heat transfer nor for the droplet interaction with the substrate and the surroundings. In addition, more importantly, no quantitative results and validations against experiment have been provided regarding the transient evolution of a freezing droplet shape. Numerically, droplet solidification is tackled by using the enthalpy formulation (Voller & Cross 1983; Voller & Prakash 1987; Pasandideh-Fard, Chandra & Mostaghimi 2002) and the numerical artefact of penalization to discriminate between the liquid and ice phases; the freezing growth angle is also another adjusting parameter considered in order to approximate experimental droplet shapes (Virozub, Rasin & Brandon 2008). Finally, it is worth noting the ongoing works on understanding supercooled water droplet impact and freezing with the effect of the surroundings or impact on an ice surface (Mohammadi *et al.* 2017; Schreimb, Roisman & Tropea 2018; Tembely *et al.* 2018), the freezing and transient evolution of the droplet exhibiting a density contrast between ice and liquid is still to be fully addressed. However, our current approach on equilibrium solidification may pave the way for a better understanding and modelling of a supercooled droplet.

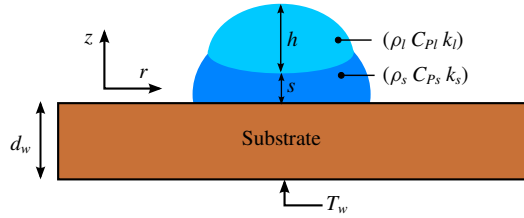


FIGURE 1. (Colour online) Geometry of the physical system of a freezing droplet on a cold substrate.

The present paper aims to develop a theoretical and numerical approach based on a one-dimensional approximation to model water droplet freezing on a cold solid surface. The formulation, in addition to shedding light on the mechanism of droplet freezing, extends the use of thin film model, used in many icing codes in the aerospace industry, beyond its conventional domain of applicability. The paper is organized as follows. In § 2 governing equations based on mass, momentum and energy conservation are derived by incorporating effects such as the disjoining pressure, full mean curvature, the contrast in physical properties between the (liquid) water and ice along with the Gibbs–Thomson effect, as well as the substrate properties. In § 3, the results and validation of the approach are detailed along with a sensitivity study of the model. Finally, conclusions are drawn in § 4.

2. Governing equations

We consider the freezing of a sessile droplet on a uniformly cooled substrate (figure 1). The liquid/gas interface is described by the profile $h(r, t)$, whereas the freezing front evolution is given by $s(r, t)$. The droplet is deposited on a substrate with an equilibrium angle θ_E , which may be reached when the droplet spreads towards its equilibrium state. The substrate on which the droplet is seated is maintained at a constant temperature, T_w , from the bottom side. The substrate has a thickness of d_w , and thermal conductivity of k_w . Since this work is concerned with phase change, the model accounts for the physical properties for each phase present, namely, the density (ρ_l, ρ_s), thermal conductivity (k_l, k_s) and heat capacity (C_{pl}, C_{ps}), which are different for the (liquid) water and (solid) ice phases. The previous assumptions make the simulation more challenging and require accounting for the physics governing the phase change in order to capture the details of droplet freezing. In addition, the model should be able to capture both the droplet shape as well as the freezing front evolution. To be general the governing equations will be derived in a three-dimensional configuration before focusing on the two-dimensional axisymmetric case for application. The liquid/gas interface is described by the profile $h(x, y, t)$, whereas the freezing front evolution is given by the $s(x, y, t)$. The model will be based on the long range approximation, derived from the Navier–Stokes equations, and the maintaining of the droplet at equilibrium is dealt with using a precursor film approach along with an adequate disjoining pressure.

2.1. Navier–Stokes equations

The liquid, assumed incompressible of density (ρ_l), surface tension (γ_l) and viscosity (μ_l), evolves following the mass and momentum conservation equations, which are

given by the Navier–Stokes equations as follows:

$$\nabla \cdot \mathbf{v} = 0, \tag{2.1}$$

$$\rho_l \left(\frac{\partial \mathbf{v}}{\partial t} + (\mathbf{v} \cdot \nabla) \mathbf{v} \right) = -\nabla p + \mu_l \nabla^2 \mathbf{v} + \rho_l g \sin \alpha \mathbf{i} - \rho_l g \cos \alpha \mathbf{k}, \tag{2.2}$$

where \mathbf{v} is the velocity, g is the gravitational acceleration; for generality the substrate may be tilted by an angle α .

In addition to the fluid flow equations, the energy conservation equation has to be solved through both the solid substrate and the droplet. The phase change is accounted for by the coupling at the (water) liquid/ice interface which makes it possible to describe the freezing front evolution.

2.2. Energy conservation equation

The heat transfer equations within the droplet for both liquid and solid phases, as depicted in figure 1, can be written as

$$\rho_J C_{PJ} \left(\frac{\partial T}{\partial t} + (\mathbf{v} \cdot \nabla) T \right) = k_J \nabla^2 T \quad J = l, s, \tag{2.3}$$

where the subscripts l, s stand for liquid and solid phases, respectively.

Under the long range approximation, these equations result in the Laplace equation, where thermal conduction is the main driving heat transfer mechanism. Regarding the heat transfer under phase change, this can be further justified by the fact that, based on the characteristic temperature difference ΔT , for example between the droplet and the substrate, the number $\Delta T C_{pl} / L_f \ll 1$, where C_{pl} , L_f are the specific and latent heat of fusion, respectively. In other words, the transient heat conduction is negligible compared to the freezing front advance, as pointed out in Ajaev & Davis (2003). Finally, for both liquid and ice, and neglecting the transient contribution, the energy equation can be simplified as follows: for the solid (ice) phase,

$$\nabla^2 T_s = 0, \tag{2.4}$$

and for the liquid phase,

$$\rho_l C_{pl} (\mathbf{v} \cdot \nabla) T = k_l \nabla^2 T. \tag{2.5}$$

The advection term kept in the liquid heat transfer equation will be detailed later on when accounting for the effect of the density contrast between the liquid and solid (ice) phases.

The coupling between (2.1), (2.2) and (2.4), (2.5) will be performed under the lubrication approximation. Hence, the momentum equations (2.2) can be simplified assuming that the inertial effect is negligible, and can be rewritten by taking $\mathbf{v} = (\mathbf{u}, w)$, with the velocity horizontal components $\mathbf{u} = (u, v)$ on the substrate plane and a perpendicular component w . In the case of a droplet under the lubrication approximation, the contact angle should be relatively low ($< 65^\circ$); therefore, our model is mainly valid for the hydrophilic configuration, even though an extension proposed in the present work makes it possible to handle droplet aspect ratios (H_0/R_0) close to 1 ($\approx 90^\circ$). Under these hypotheses, the lubrication approximation, also known

as the long range or thin film approximation, can be applied (Oron, Davis & Bankoff 1997; Alleborn & Raszillier 2004) and the Navier–Stokes equations (2.1), (2.2) can be simplified as follows:

$$\tilde{\nabla} \cdot \mathbf{u} + \frac{\partial w}{\partial z} = 0, \quad (2.6)$$

$$0 = -\tilde{\nabla} p + \mu_l \frac{\partial^2 \mathbf{u}}{\partial z^2} + \rho_l g \sin \alpha \mathbf{i}, \quad (2.7)$$

$$0 = -\frac{\partial p}{\partial z} - g \cos \alpha, \quad (2.8)$$

where $\tilde{\nabla} \bullet = (\partial \bullet / \partial x, \partial \bullet / \partial y)$ stands for the planar gradient.

Integrating the pressure (2.8) with respect to z leads to $p = -g \cos \alpha z + \text{const.}$ and, on the other hand, applying the Young–Laplace boundary condition at the liquid–air interface and accounting for the disjoining pressure Π , one can express the pressure as follows:

$$p(h + s) = -\gamma \kappa + P_0 - \Pi, \quad (2.9)$$

where κ corresponds to the curvature at the droplet surface, P_0 is the atmospheric pressure, and Π corresponds to the disjoining pressure. The disjoining pressure is present owing to the precursor film, therefore (i) avoiding the singularity at the triple line and (ii) maintaining the droplet at equilibrium on the precursor film with a well-defined contact angle. At the molecular level, this disjoining pressure arises from the molecular interaction between the two interfaces, namely solid–liquid and liquid–gas. Finally, one can find the expression for the pressure within the droplet as

$$p = -g \cos \alpha (h + s - z) - \gamma \kappa - \Pi + P_0. \quad (2.10)$$

By inserting the pressure equation in (2.7) and integrating twice with respect to z between $[s, h + s]$, we retrieve the quadratic velocity profile:

$$\mu \mathbf{u} = -\tilde{\nabla} P + \rho_l g \sin \alpha \mathbf{i} (z - s) \left[\frac{z - s}{2} - h \right], \quad (2.11)$$

where $P = -g \cos \beta (h + s) - \gamma \kappa - \Pi$. This equation is derived under the no-slip condition at the liquid–ice interface $z = s$, $\mathbf{u} = 0$, and the vanishing shear stress at $z = h + s$, $\mu_l \partial \mathbf{u} / \partial z = 0$. Finally, one can deduce the average velocity over the liquid thickness defined as

$$\mathbf{U} = \frac{1}{h} \int_s^{h+s} \mathbf{u} \, dz = -[-\tilde{\nabla} P + \rho_l g \sin \alpha \mathbf{i}] \frac{h^2}{3\mu}. \quad (2.12)$$

Knowing the velocity field in the liquid phase, we can now turn to the continuity equation of the freezing droplet. Integrating equation (2.6) with respect to z between $[s, s + h]$, we find

$$\int_s^{s+h} \tilde{\nabla} \cdot \mathbf{u} \, dz + w|_{z=h+s} - w|_{z=s} = 0. \quad (2.13)$$

Using the Leibniz integral rule,

$$\int_s^{s+h} \tilde{\nabla} \cdot \mathbf{u} \, dz = \tilde{\nabla} \cdot \int_s^{s+h} \mathbf{u} \, dz - [\mathbf{u} \tilde{\nabla} (h + s)]_{h+s} - \mathbf{u} \tilde{\nabla} s|_s, \quad (2.14)$$

and using the definition of \mathbf{U} from (2.12) and the no-slip condition at the liquid–ice interface $\mathbf{u}|_s \equiv 0$, equation (2.14) can be simplified as

$$\int_s^{s+h} \tilde{\nabla} \cdot \mathbf{u} \, dz = \tilde{\nabla} \cdot (h\mathbf{U}) - \mathbf{u} \tilde{\nabla} (h+s)|_{h+s}, \tag{2.15}$$

and finally noting that the kinematic boundary condition at the top of the droplet can be expressed as

$$w|_{z=h+s} = \frac{d}{dt}(h+s) = \frac{\partial}{\partial t}(h+s) + \mathbf{u} \tilde{\nabla} (h+s), \tag{2.16}$$

then by combining (2.13) and (2.15) into (2.16), the continuity equation can be rewritten as follows:

$$\frac{\partial}{\partial t}(h+s) + \tilde{\nabla} \cdot (h\mathbf{U}) = w|_{z=s}. \tag{2.17}$$

The right-hand side in (2.17) to be determined is the freezing front vertical speed $w|_{z=s}$, which will be expressed by exploiting the mass and energy conservation at the interface between ice and liquid, as detailed below.

2.3. Mass conservation at the freezing front

The conservation of mass between the liquid and solid phases leads to

$$\rho_l(\mathbf{v}_l - \mathbf{v}_i) \cdot \mathbf{n} = \rho_s(\mathbf{v}_s - \mathbf{v}_i) \cdot \mathbf{n}, \tag{2.18}$$

where the velocity of the solid (ice) phase is assumed to be zero, $\mathbf{v}_s \equiv 0$. The normal unit vector at the interface $\mathbf{n} = (-\partial_x s, -\partial_y s, 1)$, and the interface velocity is given by $\mathbf{v}_i = (0, 0, \partial_t s)$, hence (2.18) can be rewritten as

$$\rho_l(-u\partial_x s - v\partial_y s + w - \partial_t s) = -\rho_s\partial_t s, \tag{2.19}$$

which can be further simplified by using the no-slip condition at the interface $u \equiv v \equiv 0$:

$$w|_{z=s} = \left(1 - \frac{\rho_s}{\rho_l}\right) \frac{\partial s}{\partial t}. \tag{2.20}$$

We can see that when $\rho_s/\rho_l < 1$, there would be an expansion, and the induced velocity to the liquid phase due to expansion is positive.

Finally, inserting (2.20) in (2.17), one obtains the lubrication equation accounting for the phase change as follows:

$$\frac{\partial h}{\partial t} + \tilde{\nabla} \cdot (h\mathbf{U}) = -\frac{\rho_s}{\rho_l} \frac{\partial s}{\partial t}. \tag{2.21}$$

The source term on the right-hand side describes the conversion between ice and liquid phases during the freezing process: an increase of the ice front leads to a decrease of the liquid, and that conversion rate is controlled by the ratio of the ice and liquid density.

2.4. Energy conservation at the freezing front

In addition to the mass conservation, energy conservation at the interface has to be applied to close the problem. At the interface, the energy balance through conduction and phase change is written as

$$\rho_l H_l (\mathbf{v}_l - \mathbf{v}_i) \cdot \mathbf{n} - k_l \nabla T \cdot \mathbf{n} = \rho_s H_s (\mathbf{v}_s - \mathbf{v}_i) \cdot \mathbf{n} - k_s \nabla T \cdot \mathbf{n}. \quad (2.22)$$

Accounting for the properties of both ice and solid, the enthalpy jump at the interface corresponds to $\Delta H = H_l - H_s$, with the enthalpies $H_l = C_{pl} T_m + L_f$ and $H_s = C_{ps} T_m$ of the liquid and solid, respectively, with phase change occurring at a definite temperature (T_m). Assuming the heat transfer is dominant in the z -direction with the following condition satisfied, $\partial_x T \partial s_x \propto \partial_y T \partial s_y \ll \partial_z T$, equation (2.22) can be expressed as

$$[\rho_s L_f + (\rho_l C_{pl} - \rho_s C_{ps}) T_m] \frac{\partial s}{\partial t} = k_s \frac{\partial T_s}{\partial z} - k_l \frac{\partial T_l}{\partial z}. \quad (2.23)$$

Equation (2.23) requires solving the heat transfer equation for both the liquid and ice phase. As previously indicated in § 2.2, these equations reduce to the Laplace equation, quasi-steady approximation, which will be solved in the z -direction. The quasi-static temperature distribution provides a reasonable approximation as long as $C_{pl} \Delta T < L_f$.

2.5. Equilibrium temperature at freezing front: Gibbs–Thomson relation

Interfacial surface tension and the curvature affect the equilibrium temperature at the interface between the ice and liquid following the Gibbs–Thomson relation with the correction below for the melting temperature:

$$T_{eq} = T_m \left(1 - \frac{\gamma_{SL} \kappa_s}{\rho_s L_f} \right), \quad (2.24)$$

where γ_{SL} is the interfacial energy between ice–liquid, κ_s the curvature at the freezing front s . Therefore the boundary condition for the temperature is expressed as

$$T_l = T_s = T_{eq} \quad \text{at } z = s. \quad (2.25)$$

It is worth noting that in (2.23), the prefactor on the left-hand side term has been approximated as $(\rho_l C_{pl} - \rho_s C_{ps}) T_m (1 - \Gamma \kappa) \approx (\rho_l C_{pl} - \rho_s C_{ps}) T_m$, since $\Gamma = \gamma_{SL} / \rho_s L$ and $\rho_l C_{pl} - \rho_s C_{ps}$ are usually small for water.

Knowing the melting temperature at the liquid/solid interface, the heat flux can be evaluated considering the thermal resistance of the substrate, d_w/k_w , and the solid (ice), s/k_s , along with the thermal contact resistance, r_c , assumed between the liquid and the substrate figure 2. This contact resistance imposes a flux of $q = (T_w - T)/r_c$ at $z = 0$, on the substrate. From these considerations, one can deduce the flux at the liquid–ice interface, $z = s$, as follows:

$$q_s = -k_s \frac{\partial T_s}{\partial z} = -k_s \frac{T_{eq} - T_w}{s + d_w k_s / k_w + k_s r_c}, \quad (2.26)$$

where T_w is the temperature imposed at the bottom of the substrate located at $z = -d_w$.

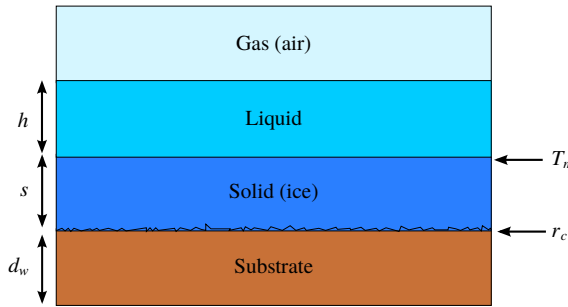


FIGURE 2. (Colour online) Schematic of the heat transfer model.

In order to find the heat flux from the liquid $q_l = -k_l \partial_z T$, we have to solve the heat transfer equation in the liquid phase:

$$\rho_l C_{pl} w_s \frac{\partial T}{\partial z} = k_l \frac{\partial^2 T}{\partial z^2}. \tag{2.27}$$

Under the quasi-static approximation, neglecting $\rho_l C_{pl} \partial_t T$ as previously explained, and taking the value for the moving interface given by (2.20), $w_s = (1 - \rho_s / \rho_l) \dot{s}$, we can deduce the equation to be verified by the temperature field within the liquid phase as

$$\frac{\partial^2 T}{\partial z^2} - \frac{\rho_l - \rho_s}{\rho_l \alpha_l} s \frac{\partial T}{\partial z} = 0, \tag{2.28}$$

where the liquid thermal diffusivity is $\alpha_l = k_l / \rho C_{pl}$. This equation is slightly different from Laplace’s equation due to the contribution of the density difference. A similar contribution accounting for the density contrast between the solid and liquid phases can be found in Carslaw & Jaeger (1959) regarding the change of volume of the Stefan problem.

In addition to (2.25), the second boundary condition, neglecting the evaporation, is the heat transfer at the liquid interface between the droplet and the surrounding air, which is assumed to follow Newton’s law of cooling as follows:

$$-k_l \frac{\partial T}{\partial z} = h_{Tc} (T - \tilde{T}_a). \tag{2.29}$$

\tilde{T}_a is the surrounding temperature at the top of the static droplet, and h_{Tc} is the heat transfer coefficient, which may account for the cooling of the initial (relatively hot) deposited droplet on the substrate before freezing. Since before depositing the droplet there is a thermal equilibrium between the substrate at T_w and the atmosphere at T_a , the temperature of the surroundings relevant for heat transfer between the droplet and the air that we consider is the one situated at a distance from the substrate corresponding to the height (H_0) of the droplet, which we denote by \tilde{T}_a . It is worth noting that this configuration is different from the convection resulting from plunging a solid sphere into a fluid at a given temperature; the deposited droplet case is different due to the presence of the substrate on which the temperature field depends. The difficulty in estimating the correct value of h_{Tc} is well known and discussed in the literature. The correlations provided in the literature, for instance in the case of a sphere, do not apply to our configuration of a deposited droplet on a cold substrate.

In order to compare our results with the experiment, one numerically determines h_{Tc} along with \tilde{T}_a (see appendix A for details). It is worth noting that the determination of this coefficient may affect the usability of the present model.

After solving (2.28), via the boundary conditions (2.25) and (2.29), one finds that the liquid heat flux in (2.23) is expressed as

$$q_l = -k_l \frac{\partial T_l}{\partial z} = \frac{-\psi k_l h_T (T_a - T_{eq})}{h_T (\exp(\psi h) - 1) + \psi k_l \exp(\psi h)}, \tag{2.30}$$

where we set for simplicity $\psi = ((\rho_l - \rho_s)/\rho_l \alpha_l) \dot{s}$, with $\dot{s} = \partial s / \partial t$.

Combining (2.26) and (2.30) into (2.23) leads to

$$\rho_s \tilde{L}_f \frac{\partial s}{\partial t} = k_s \frac{T_{eq} - T_W}{s + d_w k_s / k_w + k_s r_c} - \frac{\psi k_l h_T (T_a - T_{eq})}{h_T (\exp(\psi h) - 1) + \psi k_l \exp(\psi h)}, \tag{2.31}$$

where we denote the effective latent heat $\tilde{L}_f = L_f + T_m(\rho_l C_{pl} - \rho_s C_{ps}) / \rho_s$. The solidification models in the literature do not account for this effect, which should not be neglected since it corrects the latent heat by approximately a factor of 3. Furthermore, that correction could become important when investigating the droplet freezing time, as sought in the present work. Besides, we can simplify (2.31), noting that $\psi h \ll 1$, i.e. the contribution to the advection due the density contrast is low.

2.6. Dimensionless general equations for droplet freezing

In order to apply the model to the investigation of water droplet freezing, the governing equations will be expressed in cylindrical coordinates (r, z) and in dimensionless form for convenience. Therefore from (2.21), we deduce

$$\frac{\partial h}{\partial t} + \frac{1}{r} \frac{\partial}{\partial r} (rhU) = -\rho \frac{\partial s}{\partial t}, \tag{2.32}$$

$$U = -h^2 B_p \frac{\partial \tilde{P}}{\partial r}, \tag{2.33}$$

where $B_p = \gamma H_0^3 t_c / 3\mu R_0^4$ and the density ratio $\rho = \rho_s / \rho_l$. The coordinate r is scaled by the droplet initial radius R_0 , and the heights h and s are scaled by the droplet initial height H_0 , while the temperature is scaled by $\Delta T = T_m - T_W$, with T_m the melting temperature of water. It is worth noting that, even if the basal radius of the droplet is constant, the droplet–air interface is subject to change during the freezing process; and the description of the droplet evolution equation, equation (2.32), is essential for the numerical model to track the droplet–air interface from the onset of freezing to the tip formation. Regarding the modelling of droplet freezing, two time scales are involved: the first one (t_s) is related to droplet deformation while the freezing is concerned with the second one (t_F). These two time scales are given by

$$t_s = \frac{3\mu R_0^4}{\gamma H_0^3} \quad \text{and} \quad t_F = \frac{\rho_s \tilde{L} H_0^2}{k_s \Delta T}. \tag{2.34a,b}$$

The two characteristic times are relevant since the modelling is concerned with the freezing of a (deformable) droplet, as opposed to a static object. Only t_F would have been relevant if the freezing had to be performed on a static configuration such as

in the case of the Stefan problem. Therefore, we introduce t_c , which combines the two time scales for the modelling of the freezing droplet and defines it as the product between the two characteristic times as

$$t_c^2 = \frac{3\mu R_0^4 \rho_s \tilde{L} H_0^2}{\gamma H_0^3 k_s \Delta T} = \frac{3\mu \rho_s \tilde{L} R_0^4}{\gamma k_s H_0 \Delta T}. \tag{2.35}$$

The time scale $t_c = (3\mu \rho_s \tilde{L}_f R_0^4 / (\gamma k_s H_0 \Delta T))^{1/2}$ combines both the visco-capillary time scale $t_s = 3\mu R_0^4 / \gamma H_0^3$ and the time scale of the freezing process $t_f = \rho_s \tilde{L} H_0^2 / k_s \Delta T$. This is the time scale that accounts for the physics of our problem and is the one adopted throughout our modelling for droplet freezing. It is worth noting that the constant B_p , which overall represents the visco-capillary contribution during the freezing process, is quite dependent on our choice of the characteristic time scale. For example, by choosing $t_c = t_s$, i.e. the time is measured in the unit of the spreading time scale, then $B_p = 1$, and one retrieves the classical form for modelling droplet spreading under the lubrication approximation (Schwartz & Eley 1998).

In order to have a similar droplet shape to the experiment, the expression of the full mean curvature in the capillary and disjoining pressure contribution is adopted, which enables our model to extend the one-dimensional approximation beyond the leading-order asymptotics. By doing so, the equilibrium shape of the droplet can be retrieved as a spherical cap. The use of the full mean curvature in the one-dimensional analysis is a powerful tool to capture the nonlinear dynamics of interfacial flows, as demonstrated in Eggers (1993), Eggers & Dupont (1994) and Tembely *et al.* (2012). It is worth noting that, traditionally, the thin film model for modelling droplet spreading does not make use of the full mean curvature expression, as applied in the present work (2.36). For a partially wetted surface, a disjoining pressure accounting for the intermolecular force is added to the static pressure inside the droplet (O'Brien & Schwartz 2002; Bonn *et al.* 2009). Here the two-term disjoining pressure, corresponding to a Lennard–Jones interaction potential ($n = 9, m = 3$), in agreement with the Frumkin–Derjaguin model (Schwartz & Eley 1998) relating the static contact angle to interfacial energies, is used for the substrate wettability. The disjoining pressure prevents the thin film from thinning below the prescribed thickness h^* . Taking the full mean curvature yields the pressure contribution term as follows:

$$\tilde{P} = -\frac{1}{r} \frac{\partial}{\partial r} \frac{r(\partial_r h + \partial_r s)}{[1 + \varepsilon^2(\partial_r h + \partial_r s)^2]^{1/2}} - \Pi, \tag{2.36}$$

with $\varepsilon = H_0/R_0$, and $\Pi = A[(h^*/h)^n - (h^*/h)^m]$ with $A = (1 - \cos \theta_E)(n - 1)(m - 1)R_0^2/h^*(n - m)H_0^2$.

The disjoining pressure serves to maintain the droplet at the equilibrium position while the freezing front advances. It has little effect on the tip singularity as long as h^* is small. At isothermal conditions, a higher value of h^* causes the droplet to spread more (Schwartz & Eley 1998).

Finally, accounting for the properties of the liquid water, ice and substrate, the enthalpy jump at the interface, equation (2.31), leads to the following evolution equation for the freezing front in dimensionless form:

$$\frac{\partial s}{\partial t} = Ste \left[\frac{1 - GT}{s + W + k_s R_c / H_0} - \lambda \frac{B_i(\vartheta_a + GT)}{B_i h + 1 + \psi h} \right], \tag{2.37}$$

$\rho = \rho_s / \rho_l$	Density ratio
$\lambda = k_l / k_s$	Thermal conductivity ratio
$W = d_w k_s / H_0 k_w$	Dimensionless parameter for the substrate thermal resistance
$Ste = t_c k_s \Delta T / \rho_s \tilde{L}_f H_0^2$	Dimensionless Stefan number
$\Delta T = T_m - T_w$	Temperature scale
$Bi = h_{T_c} H_0 / k_l$	Biot number
$\vartheta_a = (T_a - T_m) / (T_m - T_w)$	Temperature ratio

TABLE 1. Main dimensionless numbers used in the model.

with $\vartheta_a = T_a - T_m / (T_m - T_w)$ and $\lambda = k_l / k_s$, while the Stefan number is defined as $Ste = t_c k_s \Delta T / \rho_s \tilde{L}_f H_0^2$, and the Biot number $Bi = h_{T_c} H_0 / k_l$. A summary of the main dimensionless parameters of the model is given in table 1. It is worth noting that a modified latent heat $\tilde{L}_f = L_f + T_m(\rho_l C_{pl} - \rho_s C_{ps}) / \rho_s$ is used in Ste , which is often not considered in the literature of solidification models. Neglecting the density and heat capacity contrast in \tilde{L}_f results in underestimating its value by almost a factor of three. Consequently, this effect is essential in order to accurately predict the water droplet features and freezing time, as considered below. In addition to the ratio of thermal conduction resistances of the substrate and the droplet $W = d_w k_s / H_0 k_w$, equation (2.37) includes the effect of the velocity induced during phase change, $\psi = (\rho_l - \rho_s) \dot{s} / \rho_l \alpha_l$, as a result of the density contrast between the liquid and ice.

Finally, the Gibbs–Thomson effect, termed GT in (2.37), yields

$$GT = \frac{(\gamma_{LS} / \rho_s \tilde{L}) T_m H_0}{R_0^2 \Delta T} \frac{1}{r} \frac{\partial}{\partial r} \left(\frac{r \partial_r s}{[1 + \varepsilon^2 (\partial_r s)^2]^{1/2}} \right). \tag{2.38}$$

The GT contribution mainly serves to ensure the convergence and stability of the numerical solution, while its actual effect on the freezing seems to be marginal.

The previous nonlinear PDEs, equations (31)–(34), are implemented and solved using the method of lines suitable for stiff initial value and nonlinear problems. The UMFPACK linear solver and a maximum backward differentiation formula (BDF) order of 5 are used since these methods have been shown to be efficient to solve such initial value stiff nonlinear partial differential equations (Sellier & Panda 2010). On the boundary of the domain, the following conditions are imposed: $\nabla P \cdot \mathbf{n} = \mathbf{U} \cdot \mathbf{n} = 0$. In one dimension, the mesh line between 0 and 2.5 is meshed with 1920 elements, and the precursor film thickness is taken as $h^* = 0.006$, which is found to be a good compromise between numerical accuracy and computational cost, while a Heaviside function is used to prevent precursor film freezing. When the droplet is assumed to be a spherical cap, the equation for the initial profile in dimensionless form $h_0(r)$ is expressed as follows:

$$h_0(r) = \sqrt{\frac{\tilde{R}}{H_0^2} - \left(\frac{R_0}{H_0}\right)^2} r^2 - \frac{\tilde{R} - H_0}{H_0}, \tag{2.39}$$

where $\tilde{R} = (H_0^2 + R_0^2) / 2H_0$, and the initial contact angle is given by $\tan \theta_0 = 2H_0 R_0 / (R_0^2 - H_0^2)$. Note that the spherical cap approximation is fully valid as long as the Bond number $Bo = \rho g H_0^2 / \gamma < 1$, or the droplet initial height (H_0) is less than the capillary length.

	Value	SI
C_{Pl}	4220	$\text{J kg}^{-1} \text{K}^{-1}$
C_{Ps}	1020	$\text{J kg}^{-1} \text{K}^{-1}$
d_W	1.5×10^{-3}	m^{-1}
γ	70×10^{-3}	N m^{-1}
γ_{LS}	20×10^{-3}	N m^{-1}
h_C	462	$\text{W m}^{-2} \text{K}^{-1}$
k_l	0.57	$\text{W m}^{-1} \text{K}^{-1}$
k_s	2.18	$\text{W m}^{-1} \text{K}^{-1}$
k_W	109	$\text{W m}^{-1} \text{K}^{-1}$
L_f	3.34×10^5	J kg^{-1}
r_c	10^{-6}	$\text{W}^{-1} \text{m}^2 \text{K}$
T_a	293.5	K
T_m	273	K
μ_l	10^{-3}	Pa s
ρ_l	1000	kg m^{-3}
ρ_s	900	kg m^{-3}
θ_E	70°	—

TABLE 2. Parameters of the simulations.

3. Results and discussion

3.1. Droplet freezing modelling

We investigated water droplet freezing at equilibrium on a cold solid substrate by solving the coupled PDEs (2.32)–(2.38). The model predictions are compared with one of the most detailed experimental results (to the best of our knowledge) of water droplet freezing, that reported in Hu & Jin (2010). A 500 μm diameter droplet is deposited on a brass substrate of 1.5 mm thickness maintained at -2°C by circulating nitrogen gas. The use of the molecular tagging thermometry techniques (TAG) enabled the authors to quantify the water droplet freezing phenomena, including the freezing front shape along with the volume expansion. The parameters used in the model are given in table 2.

In figure 3, the initial and final shapes of the frozen droplet are depicted both numerically and experimentally. The prediction of our model captures the main features of droplet freezing, such as the volume expansion and the pointy tip formation, with the tip angle at approximately 128° , close to the 130° found by Marín *et al.* (2014). However, this angle is subject to variability, which is rationalized below. It is worth noting that, initially, under our one-dimensional approximation the droplet is taken as a spherical cap, which is a good approximation due to the millimetre size of the droplet (less than the capillary length); by this choice, the governing equations (i.e. (2.32)–(2.38)) are also satisfied as a result of taking the full mean curvature (see (2.36)).

The evolution of the concave freezing front with time during the freezing is also evidenced, as highlighted in figure 4. This concave ice front is one of the features of water droplet freezing on a hydrophilic surface and is well captured by our model. Importantly, the pointy ice tip is also well retrieved.

The tip singularity, which our model retrieves, has remained a challenge in modelling solidification of water droplets. Towards the end of the solidification time (T_s), the interface shape changes and the cusp singularity appears once the

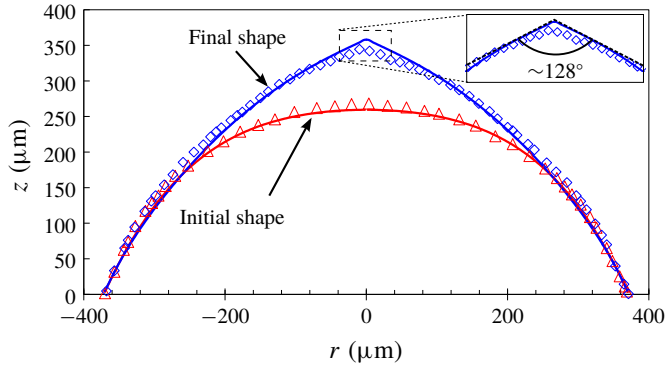


FIGURE 3. (Colour online) Experimental results (symbols) and theoretical prediction (solid line) of the initial and final, cusp-like, shape of a freezing water droplet on a solid substrate. The experimental results are from Hu & Jin (2010) who used the molecular tagging thermometry techniques (TAG) for water droplet freezing. In addition, the tip angle, of approximately 128° , is found to be in agreement with the recent finding in Marín *et al.* (2014).

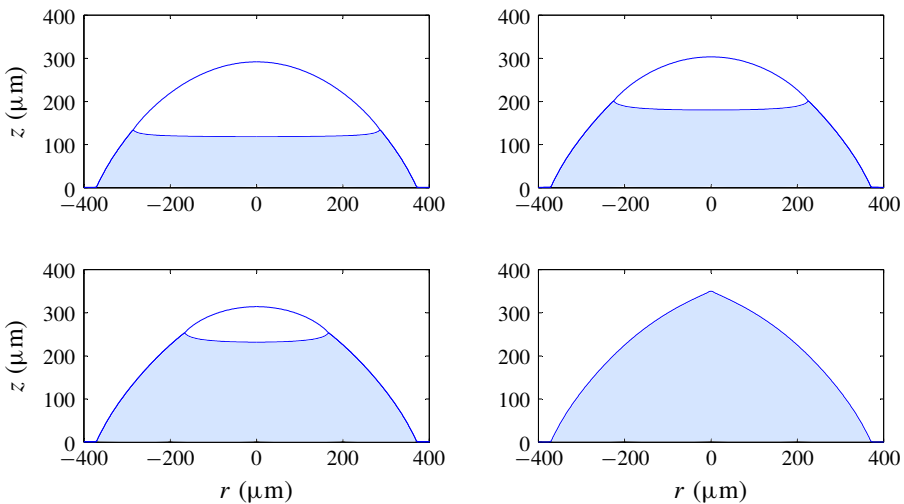


FIGURE 4. (Colour online) Evolution of predicted transient profile of a freezing droplet on a cold substrate at different times $0.2T_s$, $0.4T_s$, $0.6T_s$ and T_s , where T_s is the solidification time of the droplet.

entire droplet has turned to ice. This singularity is the result of the upward liquid expansion during the freezing process, which ultimately focuses on the tip of the droplet, leading to the pointy ice shape. In addition, it is worth noting that the unfrozen liquid part within the droplet keeps its spherical cap shape thanks to the surface tension along with the adopted full mean curvature expression.

One of the interesting parameters in droplet freezing is the solidification time, which could determine the type of ice formation, glaze or rime ice. We tested the predictive capability of our approach regarding the effect of substrate temperature on the freezing time following the same range as in Hu & Jin (2010). Using the physical

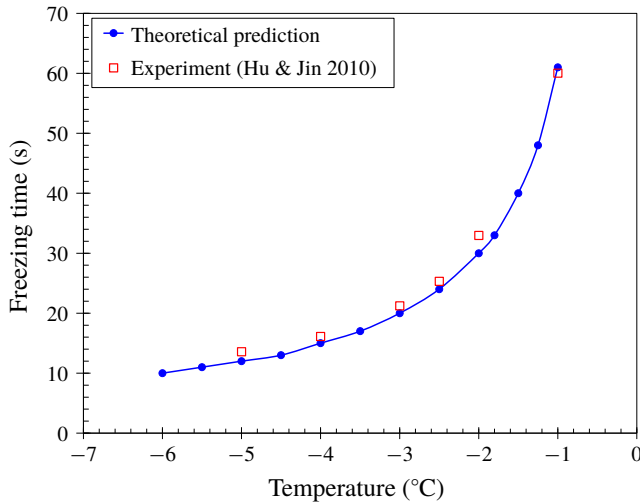


FIGURE 5. (Colour online) Effect of the substrate temperature on the freezing time.

and geometrical parameters in table 2, the comparisons between the proposed model and the experiments are very satisfactory over the range of temperatures from -2°C to -5°C as shown in figure 5. The analysis indicates that the substrate temperature is the main parameter which controls the droplet freezing time. A correlation shows that the evolution of the freezing time versus the substrate temperature follows a trend in line with the finding in Hu & Jin (2010). Interestingly, from (2.35), the choice of the freezing time $T_s \propto 1/\Delta T$ yields the freezing front evolution to be precisely an inverse function of the substrate temperature, in line with the experimental data ($T_s = 60.42\Delta T^{-0.94}$). It is worth noting that the accuracy in predicting the freezing time is highly related, as previously explained in § 2, to the fact that a modified latent heat (\tilde{L}_f) is used in the model. In addition to the operating parameter T_w , the Stefan number (Ste), based on the physical properties of the droplet, is another influencing parameter which can control water droplet freezing. In fact, the rate of phase change during the solidification phenomenon can be represented by the Stefan number, i.e. the ratio of sensible to latent heats; and we obtain in figure 6 a linear correlation between the freezing time and $1/Ste$.

Finally, in contrast to the substrate temperature, which has little effect on the freezing droplet features except the freezing time (see figure 7a), the interaction between the solidifying droplet and the surrounding medium is influenced by both the Biot number (Bi) and the temperature of the surroundings. The typical effect of Bi on the freezing front shape is illustrated in figure 7(b). The right-hand side corresponds to a Biot number 20 times higher than the one on the left-hand side. The higher the Biot number or the heat transfer rate between droplet and surroundings, the more concave upwards is the freezing front. At lower Biot number, the outer droplet surface can be considered as adiabatic and there is no heat flux entering through it, therefore the temperature gradients inside the droplet are small. However at high Bi number, the heat is evacuated at a higher rate through the droplet–air interface, which becomes cooler than the centre of the droplet; the freezing front then follows a curved isotherm freezing line. In addition, the simulation shows that the global shape of the droplet can be very much affected by the droplet heat transfer to

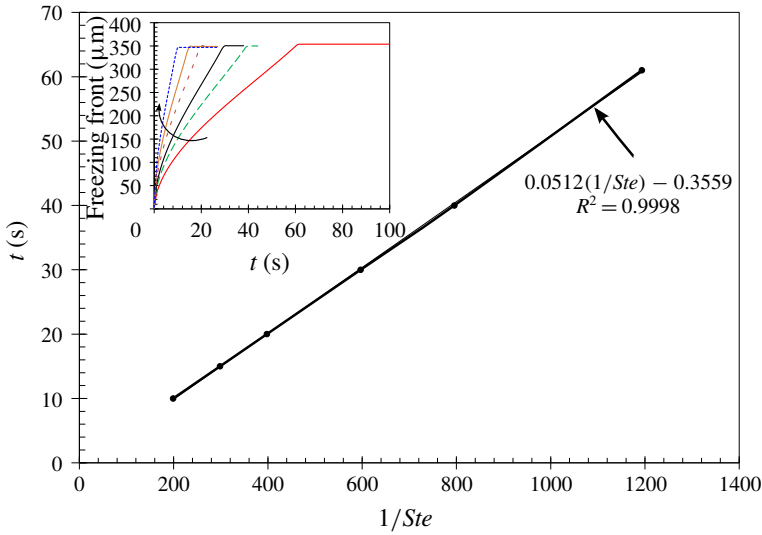


FIGURE 6. (Colour online) Numerical simulation of the freezing time with respect to the inverse Stefan number $1/Ste$. The inset corresponds to the freezing front evolution at different Stefan numbers.

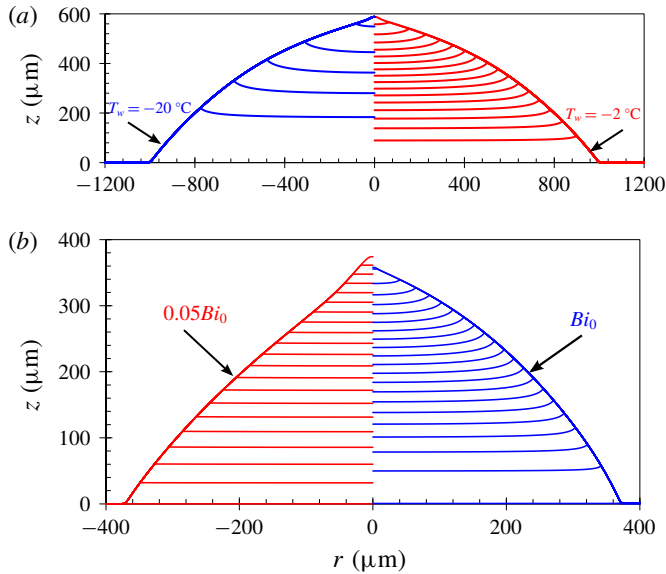


FIGURE 7. (Colour online) Comparative simulations of the effect of (a) temperature on a freezing droplet of aspect ratio $H_0/R_0 = 0.5$ and (b) the impact of the interaction between the droplet and atmosphere, as observed through the Biot number (Bi), on the freezing front shape at different stages of droplet freezing ($H_0/R_0 = 0.71$). The reference case corresponds to $Bi_0 = 0.4$. The temporal sequence, $T_f/20$, is similar in each comparative case.

the surrounding atmosphere; the frozen droplet shape at lower Bi shows an inflection while this feature seems absent from the case of higher Bi number. Furthermore, due to heat exchange between the droplet and the surroundings, the freezing front is no

longer perpendicular to the interface. This finding suggests that the tip formation universality (Marín *et al.* 2014) may not hold when accounting for the interaction with the surroundings, and this may explain the variability observed experimentally in the value of the frozen droplet tip angle in Marín *et al.* (2014).

3.2. Rationalizing the tip angle variability

Finally, based on our model, we propose to address and rationalize the variability observed in the tip angle of the frozen liquid water droplet (Marín *et al.* 2014). We provide below the derivation of the tip angle evolution, from (2.32):

$$\frac{\partial h}{\partial t} \approx -\rho \frac{\partial s}{\partial t}, \tag{3.1}$$

which leads after integration, to $h = -\rho s + \text{const}$. Initially the droplet shape is $h_0(r)$ while $s = 0$, so there is no ice formation yet, therefore $h(r, t) = -\rho s(r, t) + h_0(r)$. On the other hand, since the interface angle is given by $\partial_r[h + s] = -\tan\theta$, one can deduce

$$h'_0 + (1 - \rho)s' = -\tan\theta. \tag{3.2}$$

In order to describe the evolution of the tip angle at the final stage, one makes use of the freezing front evolution equation (2.37), neglecting however the GT effect and the induced velocity due the freezing, deriving with respect to r :

$$\frac{\partial s'}{\partial t} = Ste \left[-\frac{s'}{(s + \varpi)^2} + \lambda \frac{B_i^2 \vartheta_a h'}{(B_i h + 1)^2} \right]. \tag{3.3}$$

For simplicity, we set $\varpi = d_w k_s / h_0 k_w + k_s r_c / h_0$.

Close to the final stage of freezing, $r \rightarrow 0$, $h \rightarrow 0$, $s \rightarrow 1/\rho$, since $h_0(r \rightarrow 0) = 1$ and $h'_0(r \rightarrow 0) = 0$:

$$\frac{\partial s'}{\partial t} = Ste \left[-\frac{s'}{(1/\rho + \varpi)^2} + \lambda B_i^2 \vartheta_a h' \right]. \tag{3.4}$$

Finally the equation satisfied by s' is expressed as follows:

$$\frac{\partial s'}{\partial t} = -Ste \left[\frac{1}{(1/\rho + \varpi)^2} + \rho \lambda B_i^2 \vartheta_a \right] s'. \tag{3.5}$$

Noticing that close to the tip, $(1 - \rho)s' = -\tan\theta$, and by setting $\xi = \tan\theta$, the following equation can be written:

$$\frac{\partial \xi}{\partial t} = -Ste \left[\frac{1}{(1/\rho + \varpi)^2} + \rho \lambda B_i^2 \vartheta_a \right] \xi, \tag{3.6}$$

which can be readily solved as

$$\xi = C \exp \left[-Ste \left(\frac{1}{(1/\rho + \varpi)^2} + \rho \lambda B_i^2 \vartheta_a \right) t \right]. \tag{3.7}$$

Furthermore, close to the final stage $r \rightarrow 0$, $t - t_s \rightarrow 0$, the tip angle can be expressed by $\alpha_{tip} = \pi - 2\xi$, while $\xi = \tan \theta$ verifies the following equation:

$$\xi = \xi_0 \left[1 + Ste \left(\frac{1}{(1/\rho + \varpi)^2} + \rho \lambda B_i^2 \vartheta_a \right) (t_s - t) \right], \quad (3.8)$$

where ξ_0 corresponds to the tip angle at the final freezing time T_s , while for simplicity we set $\varpi = d_w k_s / h_0 k_w + k_s R_c / h_0$.

Interestingly, equation (3.8) may rationalize as well the seemingly uncorrelated result of figure 2(b) in Marín *et al.* (2014), where an increase of the contact angle or height-to-radius aspect ratio seems to induce a higher tip angle. In fact, by combining both the aspect ratio and the substrate temperature effects, the prefactor in (3.8) seems to predict qualitatively the correct change in the tip angle. In fact, based on the operating conditions, aspect ratio and substrate temperature in figure 2(b) from Marín *et al.* (2014), the prefactor calculation leads to $\xi_{H/R=0.46, \Delta T=20.8C} = 2.6 > \xi_{H/R=1.16, \Delta T=44.1C} = 1.1 > \xi_{H/R=4.96, \Delta T=34.4C} = 1.0$, equivalently the tip angle $\alpha_{H/R=0.46, \Delta T=20.8C} < \alpha_{H/R=1.16, \Delta T=44.1C} < \alpha_{H/R=1.16, \Delta T=44.1C}$. As can be inferred by (3.8), the interplay between all the physical parameters may rationalize the reason for the variability observed experimentally. It is worth noting that our approach, based on a scaling argument, can only provide qualitative results regarding the tip angle variability.

4. Conclusions

To conclude, we developed a comprehensive approach to the modelling of water droplet freezing on a cold solid substrate. The model is based on a one-dimensional approximation which accounts for the droplet interaction with both the substrate and the surrounding air. The governing equations are based on mass, momentum and energy conservation; and the droplet freezing is accurately modelled – without any prior assumption on the freezing growth angle – by incorporating effects such as the disjoining pressure, modified latent heat, full mean curvature expression, the Gibbs–Thomson effect, natural convection and substrate thermal and physico-chemical properties. In contrast, the physical properties of both ice and (liquid) water are used and this enables us to retrieve the main features of a freezing droplet. In addition to the freezing time, the model predicts water droplet expansion during freezing as well as the cusp singularity. The characteristic concave ice front for a freezing water droplet is also retrieved. In addition, the solidification time, which controls the type of ice, is found to evolve exponentially with the temperature. Finally, an explicit equation rationalizing the tip angle is derived and seems to explain its experimentally observed variability. The findings will have an impact on both academic and industrial approaches for accurately modelling icing phenomena.

Acknowledgements

Authors gratefully acknowledge the financial support from the Natural Sciences and Engineering Research Council of Canada (NSERC). The authors are grateful to the anonymous reviewers, whose comments have helped improve the manuscript. M.T. thanks Professor Worster for a reference suggestion.

Appendix A. Numerical determination of the heat transfer coefficient

The continuity, momentum and heat transfer equations to be numerically solved in the volume of fluid (VOF) formulation are

$$\nabla \cdot \mathbf{V} = 0, \tag{A 1}$$

$$\frac{\partial(\rho \mathbf{V})}{\partial t} + \nabla \cdot (\rho \mathbf{V} \mathbf{V}) = -\nabla p + \gamma \kappa \nabla \alpha + \nabla \cdot (\mu \nabla \mathbf{V}), \tag{A 2}$$

$$\frac{\partial(\rho C_p T)}{\partial t} + \nabla \cdot (\rho C_p T \mathbf{V}) = \nabla \cdot [\nabla(kT)]. \tag{A 3}$$

In (A 2), the continuum surface force (CSF) method of Brackbill, Kothe & Zemach (1992) is used to model the surface tension as a body force acting only on interfacial cells, and the mean curvature at the interface is given by

$$\kappa = -\nabla \cdot \left(\frac{\nabla \alpha}{|\nabla \alpha|} \right). \tag{A 4}$$

The phase fraction transport equation using the interface compression method proposed in Rusche (2003) is expressed as follows:

$$\frac{\partial \alpha}{\partial t} + \mathbf{V} \nabla \alpha + \nabla \cdot [V_c \alpha (1 - \alpha)] = 0. \tag{A 5}$$

The governing equations are implemented in C++/OpenFOAM, and the simulations (in axisymmetric geometry) are performed in parallel. The pressure implicit with splitting of operators (PISO) algorithm is used to calculate the pressure and velocity fields while the energy conservation equation is solved using a preconditioned bi-conjugate gradient technique; further details can be found in Tembely *et al.* (2018). The total heat transfer at the initial stage is deduced from a type of Newtonian cooling law,

$$T(t) = T_a + \Delta T_0 \exp(-t/\tau), \tag{A 6}$$

where the initial temperature difference between the droplet and the surroundings is $\Delta T_0 = T_{di} - \tilde{T}_a$, while the time constant $\tau = \rho_l V_d C_{pl} / h_{Ti} A_d$, with V_d and A_d the volume and surface area of the droplet, respectively. Finally, one can deduce the temperature \tilde{T}_a and the total heat transfer coefficient h_{Ti} at the initial stage, making use of τ from the slope of the graph in figure 8. While from the heat flux through the droplet interface, the local heat transfer coefficient is computed as

$$\tilde{h}_{CONV}(l) = k_l \frac{\partial T}{\partial n} \left(\frac{1}{T - \tilde{T}_a} \right), \tag{A 7}$$

and the average value expressed over the interface length l_d as

$$h_C = \frac{1}{l_d} \int_0^{l_d} \tilde{h}_{CONV}(l) dl. \tag{A 8}$$

Finally, one finds the heat transfer coefficient $h_C \approx 462 \text{ Wm}^{-2} \text{ K}^{-1}$.

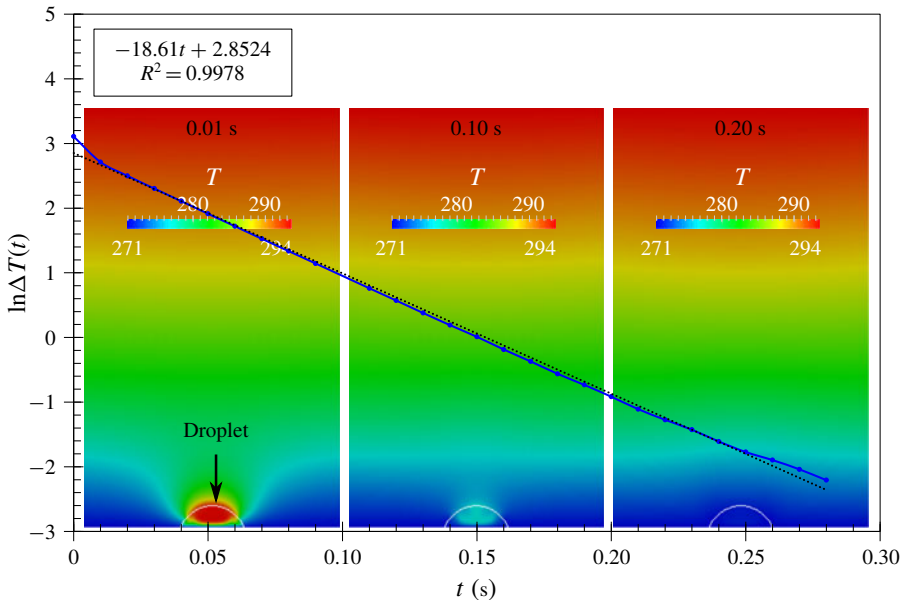


FIGURE 8. (Colour online) Numerical simulation for determining the heat transfer coefficient from a 500 μm diameter droplet at $T_{di} = 20^\circ\text{C}$ initially deposited on a cooler substrate at a fixed temperature of $T_w = -2^\circ\text{C}$.

REFERENCES

- AJAEV, V. S. & DAVIS, S. H. 2003 Boundary-integral simulations of containerless solidification. *J. Comput. Phys.* **187** (2), 492–503.
- AJAEV, V. S. & DAVIS, S. H. 2004 The effect of tri-junction conditions in droplet solidification. *J. Cryst. Growth* **264** (13), 452–462.
- ALLEBORN, N. & RASZILLIER, H. 2004 Spreading and sorption of droplets on layered porous substrates. *J. Colloid Interface Sci.* **280** (2), 449–464.
- ANDERSON, D. M., WORSTER, M. G. & DAVIS, S. H. 1996 The case for a dynamic contact angle in containerless solidification. *J. Cryst. Growth* **163** (3), 329–338.
- BONN, D., EGGERS, J., INDEKEU, J., MEUNIER, J. & ROLLEY, E. 2009 Wetting and spreading. *Rev. Mod. Phys.* **81**, 739–805.
- BRACKBILL, J. U., KOTHE, D. B. & ZEMACH, C. 1992 A continuum method for modeling surface tension. *J. Comput. Phys.* **100** (2), 335–354.
- CARSLAW, H. S. & JAEGER, J. C. 1959 *Conduction of Heat in Solids*, pp. 282–296. Oxford University Press.
- DELPLANQUE, J.-P. & RANGEL, R. H. 1997 An improved model for droplet solidification on a flat surface. *J. Mater. Sci.* **32** (6), 1519–1530.
- EGGERS, J. 1993 Universal pinching of 3D axisymmetric free-surface flow. *Phys. Rev. Lett.* **71**, 3458–3460.
- EGGERS, J. & DUPONT, T. F. 1994 Drop formation in a one-dimensional approximation of the Navier–Stokes equation. *J. Fluid Mech.* **262**, 205–221.
- ENRÍQUEZ, O. R., MARÍN, Á. G., WINKELS, K. G. & SNOEIJER, J. H. 2012 Freezing singularities in water drops. *Phys. Fluids* **24** (9), 091102.
- HAO, P., LV, C. & ZHANG, X. 2014 Freezing of sessile water droplets on surfaces with various roughness and wettability. *Appl. Phys. Lett.* **104** (16), 161609.
- HU., H. & JIN, Z. 2010 An icing physics study by using lifetime-based molecular tagging thermometry technique. *Intl J. Multiphase Flow* **36** (8), 672–681.

- JUNG, S., TIWARI, M. K., DOAN, N. V. & POULIKAKOS, D. 2012 Mechanism of supercooled droplet freezing on surfaces. *Nature Commun.* **3**, 615–622.
- MADEJSKI, J. 1976 Solidification of droplets on a cold surface. *Intl J. Heat Mass Transfer* **19** (9), 1009–1013.
- MARÍN, A. G., ENRÍQUEZ, O. R., BRUNET, P., COLINET, P. & SNOEIJER, J. H. 2014 Universality of tip singularity formation in freezing water drops. *Phys. Rev. Lett.* **113**, 054301.
- MESSINGER, B. L. 1953 Equilibrium temperature of an unheated icing surface as a function. *J. Aeronaut. Sci.* **20**, 29–41.
- MOHAMMADI, M., TEMBELY, M. & DOLATABADI, A. 2017 Predictive model of supercooled water droplet pinning/repulsion impacting a superhydrophobic surface: the role of the gas–liquid interface temperature. *Langmuir* **33** (8), 1816–1825.
- MYERS, T. G. & CHARPIN, J. P. F. 2004 A mathematical model for atmospheric ice accretion and water flow on a cold surface. *Intl J. Heat Mass Transfer* **47** (25), 5483–5500.
- MYERS, T. G., CHARPIN, J. P. F. & CHAPMAN, S. J. 2002 The flow and solidification of a thin fluid film on an arbitrary three-dimensional surface. *Phys. Fluids* **14** (8), 2788–2803.
- O'BRIEN, S. B. G. & SCHWARTZ, L. W. 2002 Theory and modeling of thin film flows. In *Encyclopedia of Surface and Colloid Science* (ed. A. Hubbard), pp. 5283–5297. Dekker.
- ORON, A., DAVIS, S. H. & BANKOFF, S. G. 1997 Long-scale evolution of thin liquid films. *Rev. Mod. Phys.* **69**, 931–980.
- ÖZGEN, S. & CANIBEK, M. 2008 Ice accretion simulation on multi-element airfoils using extended messenger model. *Heat Mass Transfer* **45** (3), 305–322.
- PASANDIDEH-FARD, M., CHANDRA, S. & MOSTAGHIMI, J. 2002 A three-dimensional model of droplet impact and solidification. *Intl J. Heat Mass Transfer* **45** (11), 2229–2242; 00218.
- POTAPCZUK, M. 2013 Aircraft icing research at NASA Glenn Research Center. *J. Aerosp. Engng* **26**, 260–276.
- RUSCHE, H. 2003 Computational fluid dynamics of dispersed two-phase flows at high phase fractions. PhD thesis, Imperial College London (University of London).
- SCHREMB, M., ROISMAN, I. V. & TROPEA, C. 2018 Normal impact of supercooled water drops onto a smooth ice surface: experiments and modelling. *J. Fluid Mech.* **835**, 1087–1107.
- SCHULTZ, W. W., WORSTER, M. G. & ANDERSON, D. M. 2001 Solidifying sessile water droplets. In *Interactive Dynamics of Convection and Solidification* (ed. D. S. R. P. Ehrhard & P. H. Steen). Kluwer.
- SCHWARTZ, L. W. & ELEY, R. R. 1998 Simulation of droplet motion on low-energy and heterogeneous surfaces. *J. Colloid Interface Sci.* **202** (1), 173–188.
- SELLIER, M. & PANDA, S. 2010 Beating capillarity in thin film flows. *Intl J. Numer. Meth. Fluids* **63** (4), 431–448.
- SNOEIJER, J. H. & BRUNET, P. 2012 Pointy ice-drops: how water freezes into a singular shape. *Am. J. Phys.* **80** (9), 764–771.
- TEMBELY, M., ATTARZADEH, R. & DOLATABADI, A. 2018 On the numerical modeling of supercooled micro-droplet impact and freezing on superhydrophobic surfaces. *Intl J. Heat Mass Transfer* **127**, 193–202.
- TEMBELY, M., VADILLO, D., MACKLEY, M. R. & SOUCEMARIANADIN, A. 2012 The matching of a one-dimensional numerical simulation and experiment results for low viscosity Newtonian and non-Newtonian fluids during fast filament stretching and subsequent break-up. *J. Rheol.* **56** (1), 159–183.
- VIROZUB, A., RASIN, I. G. & BRANDON, S. 2008 Revisiting the constant growth angle: estimation and verification via rigorous thermal modeling. *J. Cryst. Growth* **310** (24), 5416–5422.
- VOLLER, V. & CROSS, M. 1983 An explicit numerical method to track a moving phase change front. *Intl J. Heat Mass Transfer* **26** (1), 147–150.
- VOLLER, V. R. & PRAKASH, C. 1987 A fixed grid numerical modelling methodology for convection–diffusion mushy region phase-change problems. *Intl J. Heat Mass Transfer* **30** (8), 1709–1719.
- ZADRAŽIL, A., STEPANEK, F. & MATAR, O. K. 2006 Droplet spreading, imbibition and solidification on porous media. *J. Fluid Mech.* **562** (33), 1–33.
- ZHANG, H., WANG, X. Y., ZHENG, L. L. & SAMPATH, S. 2004 Numerical simulation of nucleation, solidification, and microstructure formation in thermal spraying. *Intl J. Heat Mass Transfer* **47** (10–11), 2191–2203.